ADVANCED FUNCTIONAL MATERIALS
www.afm-journal.de

A Spider´s Fang: How to Design an Injection Needle Using Chitin-Based Composite Material

Yael Politi, Matthias Priewasser, Eckhard Pippel, Paul Zaslansky, Jürgen Hartmann, Stefan Siegel, Chenghao Li, Friedrich G. Barth, and Peter Fratzl*

Spiders mainly feed on insects. This means that their fangs, which are used to inject venom into the prey, have to puncture the insect cuticle that is essentially made of the same material, a chitin-protein composite, as the fangs themselves. Here a series of structural modifications in the fangs of the wandering spider *Cupiennius salei* are reported, including texture variation in chitin orientation and arrangement, gradients in protein composition, and selective incorporation of metal ions (Zn and Ca) and halogens (Cl). These modifications influence the mechanical properties of the fang in a graded manner from tip to base, allowing it to perform as a multi-use injection needle that can break through insect cuticle, which is made of a chitin composite as well.

1. Introduction

The arthropod cuticle is a fascinating multifunctional material.[1] As an ordered fibrous composite, it serves as skin, protective shielding and skeleton, and even forms specialized working tools and sensory organs. Its structure and composition must therefore be particularly versatile, making it possible to adapt to the desired mechanical properties needed for each of its different functions. In this study we investigated the relationship between the microstructure, chemical composition, and mechanical performance of the cheliceral fangs of the wandering spider *Cupiennius salei* (**Figure 1**, for further in-depth information see ref. [2]). *C. salei* mainly feeds on insects. Therefore, its fangs have to puncture and cut through insect cuticle, made of similar material, in order to inject the venom to paralyze its prey. The fangs may thus be considered to be injection needles (≈1.5–3 mm long) with a single opening of the venom canal on the dorsal side 100–200 μm from the tip, depending on the fang's length (Figure 1B,C). Two serrated ridges run down the concave ventral side of each fang from below the canal opening halfway down the fang (Supporting Information Figure 1). The fangs must be sufficiently tough to withstand the initial impact of a rapid attack, while at the same time they need to be hard and stiff to be able to break the prey's protective cuticle.

The typical arthropod exoskeletal cuticle has two distinct parts: the epicuticle and the procuticle. The latter includes the chitin-containing layers: the exo- and endocuticle.[1,4,5] The two main components common to all arthropod cuticles, including arachnids (among them the spiders), insects and crustaceans, are α-chitin (polyacetylglucosamine), typically arranged into crystalline fibrils ≈3 nm wide and 300 nm long, and a protein matrix. This matrix is composed of tens to hundreds of different proteins,[6,7] many of which are post-translationally modified.[8] Examination of different members of the arthropod phylum shows that many of the matrix proteins contain conserved sequences[8,9] that form specific chitin–protein interactions.[6,7,10–12] Certain protein domains are involved in protein–protein interaction mostly by specific recognition motifs or cross-linking.[13] The composition of the cuticle in different functional regions exhibits variation in the chitin to protein ratio, as well as differences in the amount and type of cross-linking and the content of adsorbed water. The chitin-protein microfibers are arranged as layered sheets parallel to the cuticle surface, with the orientation of the fiber long axis varying between sheets, to form a plywood structure.[4,14,15] A stack of sheets in which the sum of rotation angles is 180° is termed a lamella. The lamella thickness (number of stacked sheets) differs significantly between different areas of the cuticle.[4,14] In a fiber-reinforced material such as the arthropod cuticle, fiber orientation is a primary factor determining the directionality of the mechanical properties.[4,16] Consequently, structural

Dr. Y. Politi, Dr. P. Zaslansky, Dr. S. Siegel, Dr. C. Li, Prof. P. Fratzl
Department of Biomaterials
Max Planck Institute of Colloids and Interfaces
14424 Potsdam, Germany
Email: yael.politi@mpikg.mpg.de

M. Priewasser
Institute of Lightweight Design and Structural Biomechanics
Vienna University of Technology
Vienna, Austria

Dr. E. Pippel
Max Planck Institute of Microstructure Physics
06120 Halle/Saale, Germany

Dr. J. Hartmann
Department of Colloid Chemistry
Max Planck Institute of Colloids and Interfaces
14424 Potsdam, Germany

Prof. F. G. Barth
Department of Neurobiology, Life Sciences
University of Vienna
Vienna, Austria

DOI: 10.1002/adfm.201200063

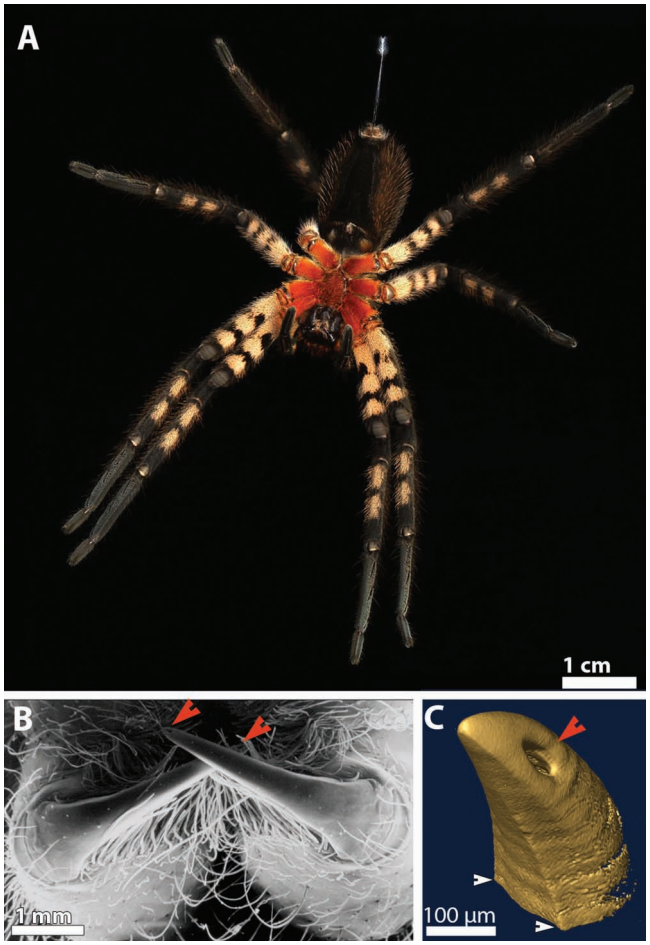

Figure 1. A) The wandering spider *Cupiennius salei* Keys. Reproduced with permission.[3] Copyright 2002, Elsevier. B) SEM image showing the spider's chelicerae with the fangs. Orange arrows point to the opening of the venom canal. C) The tip of the fang as reconstructed by µ-computer tomography. Orange arrow points to opening of venom canal. White arrow-heads mark the two reinforcement ridges that run down up to one half of the fang's length.

variations in addition to compositional changes result in huge differences in the tissue properties, with reports of up to two-thousand fold differences in the cuticle stiffness (Young's modulus).[16] Despite this known variability in cuticle properties, it is still not clear how *C. salei* modifies its chitin-based tissues so as to allow it to impact and perforate the chitinous exoskeleton of insects. The goal of the present work is to describe the structural and chemical adaptations of the spider fang cuticle, and to identify the modifications that are necessary to generate an efficient injection needle which allows puncturing prey cuticles that are similarly composed of chitin and protein.

2. Results

2.1. Microstructure

Scanning electron microscopy (SEM) and light microscopy revealed details of the three main layers of the cuticle: the epi-, exo- and endocuticle. In order to determine the boundary between exo- and endocuticle, samples taken from whole animals were compared with the fang's exuvia (naturally shed cuticle, containing only the epi- and exocuticle). All layers exhibit gradients in both morphology and thickness that vary from the fang tip (Figure 1C) to its base.

The edge of the fang tip, about 10–15 µm thick (Supporting Information **Figure 2**A–C) contains only epicuticular material, composed of globules 10–50 nm in diameter. In most other parts of the fang, the epicuticle thickness is thinner (<10 µm) (Figure 2B,C). The surface of the fang tip is covered with many small openings (Figure 2B) that are continuous with the rich pore-canal system that runs parallel to the long axis of the fang. This canal system is however structurally unrelated to the venom canal (data not shown), and the individual pore-canals bend towards the surface only proximal to the opening of the venom canal.

Beneath the epicuticle, high-resolution imaging reveals the outer layer of the exocuticle: a 10 µm thick dense lamellar structure (Figure 2D), with each of the thin lamellae only approximately 300 nm thick. This lamellar structure forms one of the two layers of the exo-cuticle, and its thickness and morphology do not change throughout the entire length of the fang. At high magnification it can be seen that the chitin fibers are coated by a thick globular matrix (**Figure 3**D-2).

The second, inner layer of the exocuticle, beneath the dense lamellar layer, exhibits a unique morphology of large columns of densely packed fibers (Figure 2E, Supporting Information Figure 2M-O). This component of the exocuticle is observed 20 µm beneath the fang tip and extends downwards approximately half of the fang length. Overall, the thickness of the exocuticle increases from about 10 µm in the vicinity of the fang tip to about 100 µm at the fang base.

Note that we do not differentiate between the endo- and the mesocuticle here, which persists in adult spiders even in hard parts of the exoskeleton and forms an intermediate stage of the sclerotizing procuticle. The definition of endo-, meso-, and exocuticle rests on Mallory's connective tissue stain where the exocuticle is the chromophobe layer and the meso- and endocuticle stain red (acid fuchsin) and blue (aniline blue), respectively. Under the transmission electron microscope meso- and endocuticle look the same and both differ from the exocuticle by their thicker lamellae.[4,17]

Inwards and adjacent to the inner layer of the exocuticle, the endocuticle is found, where the fiber architecture exhibits a typical plywood structure composed of lamellae 1–1.3 µm in thickness (Figure 3D-3). The protein-coated chitin fibers are clearly seen, but the fibers lack the thick protein coating seen in the outer layer of the exocuticle.

Diffraction and scattering patterns were acquired using a beam of 10 µm in diameter at different levels along the length of the fang. We describe in detail the results obtained from two regions at the tip of the fang, both above the opening of the venom canal: one region 10 µm below the edge of the fang's tip (Figure 3, region 1), and at a short distance (≈20 µm) beneath region 1 (Figure 3, region 2), and a third region at about midway along the fang (Figure 3, region 3). The limited resolution of this data does not allow us to unequivocally distinguish between measurements made on the epi- and exo-cuticle. We

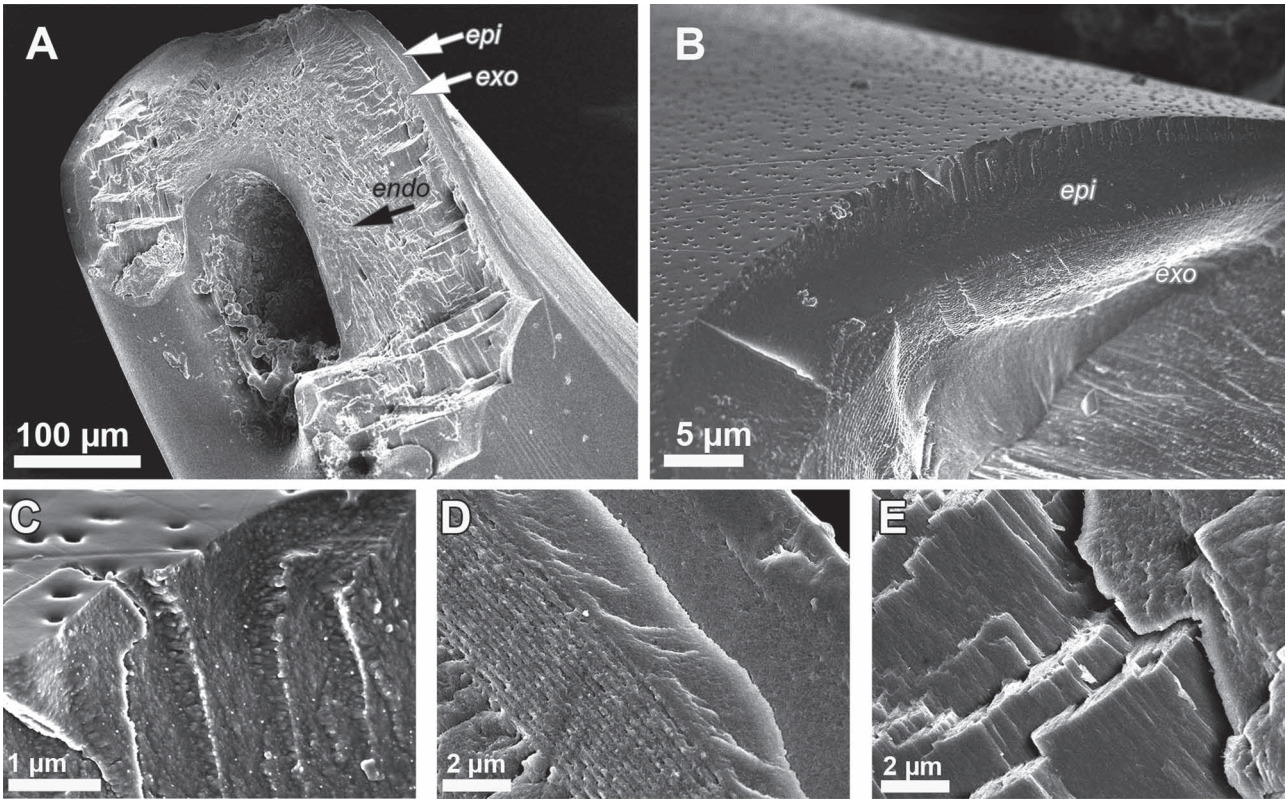

Figure 2. SEM images of a fracture surface of the fang. A) A fracture through the venom canal opening and B) on the dorsal side, to the right of the canal opening. Note many small pore-canals in (B). The epi-, exo- and endocuticle can clearly be seen. C) High magnification image of the epicuticle, showing the texture of the protein globules. The surface shows multiple small openings of the pore canals. D) High magnification image of the external layer of the exocuticle with its dense lamellar structure. Note "amorphous" epicuticle on the right. E) High magnification image of the inner layer of the exocuticle with chitin fiber bundles oriented along the long axis of the fang.

therefore simplify and hereafter refer to the "outer" and "inner" layers only.

Chitin crystals were readily identified in diffraction patterns at positions of the cuticle where fibers were also observed by other methods (e.g. SEM). Overall, we noted that the intensity of the signal of the crystalline chitin in the X-ray diffraction (XRD) patterns (Figure 3A) correlates with small angle X-ray scattering (SAXS) pattern signatures of fibrous cuticular texture (Figure 3B). At the tip of the fang (the most distal 10 µm) no chitin diffraction or fibrous SAXS pattern could be detected, suggesting that the fang tip is composed essentially of proteinaceous material (data not shown). 10 µm beneath this zone (Figure 3, region 1), the SAXS signal across the full fang width (≈30 µm) revealed two distinct textures, making it possible to differentiate between outer and inner structural layers. SAXS data of points on the peripheral regions exhibit sharp anisotropy with a streak and a weak SAXS maximum at $Q = 1.47$ nm^{-1}, where $Q = 4\pi \sin(\theta)/\lambda$, 2θ is the scattering angle, and λ is the incident beam wavelength (d-spacing = $2\pi/Q = 4.27$ nm). We interpret the streak as arising from the laminate structure of the highly ordered exocuticle that is found within the outer regions of our scan, although the chitin content is insufficient to generate characteristic diffraction peaks. The SAXS signal of the inner layer is completely isotropic with no evident SAXS peaks, and no trace of chitin was observed in the XRD patterns.

The line scan across region 2 (about 50 µm long) was obtained ≈20 to 30 µm below the fang tip. Points along this line corresponding to the outer region of the fang exhibit an anisotropic sharp maximum at $Q = 1.26$ nm^{-1} (d-spacing = 4.98 nm) that we attribute to the first order fiber packing peaks of chitin. The signal is dominated by protein scattering (Figure 3B-2). The SAXS signal of the inner layers similarly shows the anisotropic sharp maximum at $Q = 1.26$ nm^{-1}, and a second order peak is also evident at $Q = 2.52$ nm^{-1}. Correspondingly, XRD measurements of the inner layer show clear chitin diffraction peaks that are superimposed on a high background signal, presumably the amorphous proteinaceous phase (Figure 3A, curve 2).

The line scan across region 3 (800 µm long), reveals a high chitin content at the measured points located both in the inner and the outer parts of the fang cross section. The chitin diffraction peaks in the inner layer are sharp, with an additional peak seen at $Q = 6.22$ nm^{-1} in addition to the reflection from the (020) crystal plane of chitin seen at $Q = 6.6$ nm^{-1} ($d = 0.95$ nm, Figure 3A curve 3). This peak can be attributed to chitin binding proteins that are arranged regularly along the chitin crystals.[11] The chitin fiber-packing peak is shifted to higher values of Q (1.3 nm^{-1}), corresponding to a slightly denser

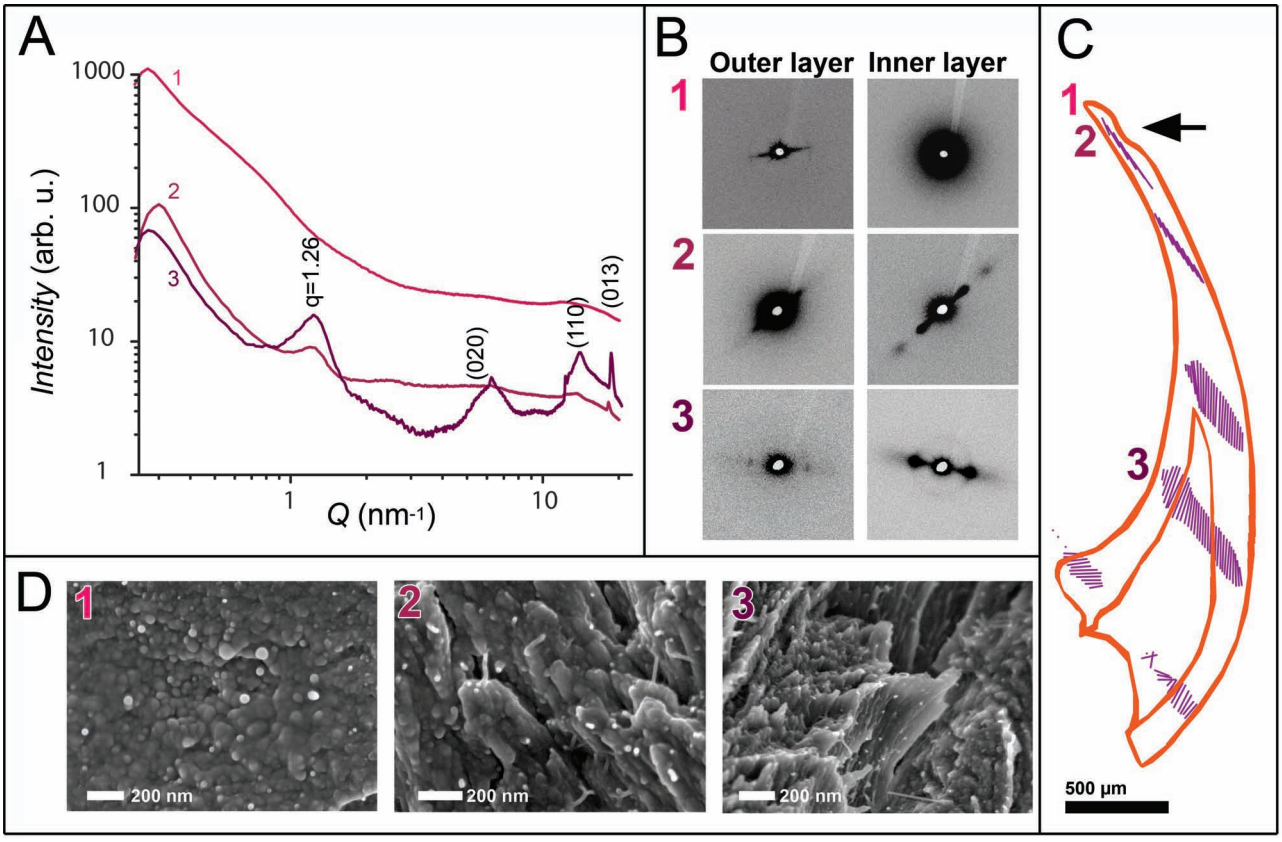

Figure 3. Material texture at different locations of the fang. A) Typical X-ray scattering and diffraction plot of the inner part of the fang, at regions 1, 2, and 3 marked on the fang contour in (C) and taken with a 10 µm focus beam. Chitin signal shows up in 2 and 3, while the signal in 1 is dominated by protein scattering. B) SAXS 2D patterns of the inner and outer layers (at the same regions (1-3). C) A vector diagram of the Rho-parameter overlaid on the outer contour of the scanned longitudinal section of the fang. The Rho-parameter was calculated using the fiber-packing SAXS peak. The length of each vector is related to the fraction of aligned fibers, and its orientation indicates the orientation of the fibers' long axes. Black arrow points to the venom canal opening. D) SEM images at areas corresponding to region 1–3 from which XRD/SAXS data are obtained: D1) the inner layers at the tip end; note the globular texture of the protein matrix at the tip edge; D2) external layer of the exocuticle with chitin fibers coated by a thick protein matrix; and D3) at the base of the fang, where the chitin fibers have a thin protein coating only. The lamellar arrangement can also be seen.

packing as compared to that seen in region 2 (d = 4.83 vs. 4.98 nm).

The fiber-packing SAXS peak was used to calculate the ρ-parameter, which is a measure of the degree of fiber alignment and orientation, where $\rho = 1$ represents fully aligned fibers and $\rho = 0$ their random orientation (within the plane of observation).[18] A schematic drawing depicting the overall fiber alignment over five line scans is shown in Figure 3C in a vector diagram overlaid on a sketch of the outer contour of the scanned longitudinal-section of the fang. The length of each vector is proportional to the fraction of co-aligned fibers (ρ parameter), and its direction indicates the averaged preferential orientation of the fiber axes. Overall, for data points from peripheral parts of the fang near the edge of each line-scan, the fiber orientation is not defined, which implies either an isotropic arrangement or a low fiber content. The inner regions show that the fibers in the fang are preferentially aligned along the fang main axis. The degree of co-alignment varies somewhat, with $\rho = 0.3$ seen closer to the fang tip, suggesting that only about 30% of the fibers are co-aligned here. Equivalent data from line scans below the venom canal opening and in region 3 reveal the highest degree of alignment with $\rho = 0.4$. Towards the base ρ decreases to 0.23.

2.2. Mechanical Properties

Scanning acoustic microscopy (SAM) (**Figure 4**, Supporting Information Figure 3) and nanoindentation measurements (**Table 1**) were performed on both longitudinal and cross-sections of the fang to map local variations in the mechanical properties. The comparison between measurements performed on longitudinal and cross-sections confirms that the fiber orientation is a primary factor determining the mechanical properties of the materials making up the fangs (Table 1). Measurements across fiber orientations in longitudinal sections (LS in Table 1) reveal significantly lower stiffness than measurements along the fiber axis in cross-sections (CS in Table 1).

The mechanical properties of the thin outer fang regions determined by both methods show little variation between measurement of cross- and longitudinal sections. This is

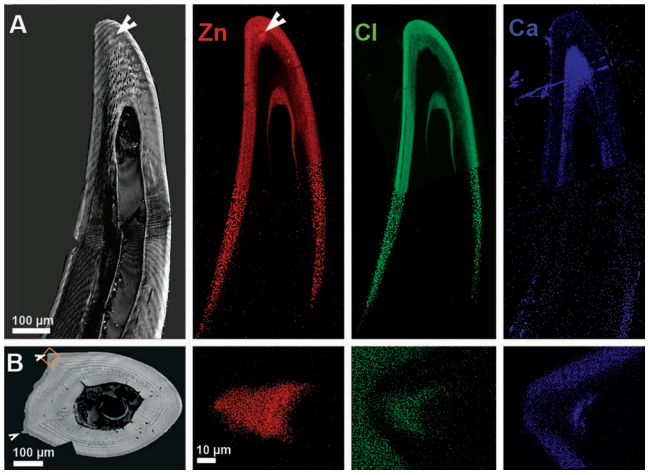

Figure 4. A) SAM image of a longitudinal section of the fang and the Zn (red), Cl (green), and Ca (Blue) distribution maps from EDX measurements. The different grey levels in the SAM images correspond to acoustic reflectivity. The arrowhead points to a spot ca. 40 µm wide of higher reflectivity, where also a higher concentration of Zn is observed without concomitant increase in Cl. In the EDX maps, long acquisition maps of the tip region are superimposed on short acquisition maps of the lower half of the fang. The striped pattern in the SAM map results from surface waves of the sample occurring during the measurement. B) SAM map of a cross section of the fang in the mid-range of its length. White arrowheads point to the two reinforcement ridges. Zn (red), Cl (green) and Ca (blue) EDX maps of a highly magnified picture of the upper ridge in the SAM image are shown. The epicuticle at this height of the fang is rich in Ca, while the reinforcement ridges are rich in Zn and Cl.

consistent with the isotropic texture revealed by our microstructural observations. At a distance of about 100 µm from the fang tip and distal to the opening of the venom canal, the measured indentation moduli are substantially higher in cross-sections (load parallel to fiber axis) than in longitudinal section (load perpendicular to fiber axis). The values are also considerably higher than in regions proximal to the opening of the venom canal. Overall, the hardness and stiffness of the cuticle of the fang decrease steeply when evaluated from its tip towards its base. Both reduced indentation modulus (*Er*) and hardness (*H*) are lowest at the base, where in both the inner and outer aspects of the fang they attain almost half their maximum values only ($H_{tip} \approx 1.3$, $H_{base} \approx 0.6$; $Er_{tip} = 20$, $Er_{base} = 13$ GPa; see Table 1).

Interestingly, the highest values of hardness and stiffness are found at the fang tip, where we found no or little chitin. Furthermore, regions of higher fiber co-alignment (Figure 3) do not necessarily correlate with higher modulus values. The mechanical property variations in the fang thus cannot be explained solely based on the protein-chitin ratio or variations of the fiber orientation.

2.3. Chemical Composition

Element analysis by X-ray fluorescence (XRF) reveals the presence of various transition metals (Zn, Fe, Cu, Mn, and Ca). According to XRF measurements (data not shown) Zn is highly concentrated in the distal tip of the fang, together with small amounts of Fe and Cu. However, in energy dispersive X-ray spectroscopy (EDX), the latter two were not detected, implying that their concentration is lower than 1 wt%. Similarly, Mn was detected by XRF co-localized with Ca, but was not detected by EDX. EDX, however, reveals the presence of chlorine, which due to its low fluorescence energy cannot be detected by our XRF measurements that are performed in air. Following a detailed investigation of the distribution of Zn, Ca, and Cl using EDX, Zn, and Ca are mutually exclusive, while Zn and Cl often appear together, but with the molar ratio (Zn:Cl) varying between 1:1 and 5:1 (white arrows in Figure 4A) and even 10:1 (data not shown). The tip of the fang is both rich in Zn and Cl (maximum: up to 10 and 6 at%, respectively). Zn and Cl are also present in the epi-cuticle surrounding the fang, from the tip up to a distance of approximately 750 µm distal from the tip (Figure 4A). In the region above the canal opening, Ca of up to 2 at% is localized in the endo-cuticle. It becomes dominant in the epicuticle from about 750 µm beneath the tip where it reaches levels of 3 at%. Interestingly, the two serrated ridges of the fang (white arrows in Figure 1C) are also rich with Zn and Cl (Figure 4B).

Table 1. Mechanical properties obtained from nano-indentation (standard deviation). Pink shading: regions enriched with Zn/Cl; blue shading: enriched with Ca; white: no metal associated. * indicates regions above the opening of the venom canal. CS = cross-sections, LS=longitudinal sections.

	Distance from Tip [µm]	Inner part		Outer layer	
		CS	LS	CS	LS
Hardness [GPa]	50*	1.36 (0.2)	1.27 (0.4)	1.36 (0.2)	1.23 (0.5)
	130*	0.84 (0.3)	0.89 (0.3)	1.34 (0.3)	1.1 (0.4)
	160*	0.7 (0.1)	0.8 (1.3)	0.9 (0.2)	0.93 (0.3)
	1500	0.64 (0.1)	0.55 (0.1)	0.74 (0.1)	0.78 (0.1)
	2500	0.58 (0.2)	0.5 (0..2)	0.66 (0.1)	0.53 (0.1)
Stiffness (indentation-modulus) [GPa]	50*	20 (1.7)	21 (5)	20 (1.7)	21 (5)
	130*	21 (4.3)	16 (4)	22 (3)	19 (4)
	160*	14 (4)	12 (1.3)	15 (2)	15 (3.4)
	1500	14 (1.6)	9 (1)	15 (1.8)	11.6 (1)
	2500	13 (2.8)	10 (1.4)	12 (1.5)	11 (2)

Figure 4 and Supporting Information Figure 3 show correlations between the SAM images and the levels of Ca, Zn, and Cl. It is clear that the presence of the transition metals and of Cl contributes to the acoustic reflectivity. In addition, nanoindentation results (Table 1) show that both the reduced indentation modulus and the hardness are increased in regions of high Zn and Cl content, while Ca correlates with increased hardness relative to areas with no metal incorporation. Notably, Ca correlates with both increased hardness and increased acoustic reflectivity (Table 1 and Supporting Information Figure 3) despite its presence in relatively low concentrations.

2.4. Metal Distribution in 3D

Identical cross sectional samples were analysed first by SAM followed by nanoindentation and thereafter by SEM/EDX to minimize sample damage by the latter techniques. In specific regions near the fang tip, significantly brighter regions that were clearly evident in the SAM images (see e.g,. arrows in Figure 4A) correlated with increased levels of Zn of up to 25 at% as identified by EDX without concomitant increase in the concentration of Cl (Figure 4A). To better understand the 3D distribution of these ions in the fang, we used high-resolution monochromatic (synchrotron) X-ray microtomography (μCT) and examined differences in the attenuation throughout the fang. Well-defined regions of increased absorption contrast (corresponding to an increased electron density) were observed in the tip region. They correlated with the regions identified by EDX to contain high levels of Zn. **Figure 5**A shows a series of 2D virtual slices extracted from the reconstructed 3D volume data of the fang. When the attenuation signal is projected and integrated across the tomogram volume (Figure 5B), the distribution and localization of the high Zn containing regions are revealed. The Zn rich zone appears as an internal cap with extended protuberances anchoring it to the chitin scaffold (see video in Supporting Information). High resolution *Z*-contrast scanning-transmission electron microscopy (HR-STEM) further reveals the presence of Zn–rich granules, sized 100–200 nm in diameter, embedded in the matrix of chitin and Zn-containing proteins. High resolution images of these granules show lattice fringes and electron diffraction patterns that correspond to crystalline ZnO, and the oxygen concentration, measured by high resolution EDX, closely matches that of the Zn distribution. The presence of ZnO nanoparticles has been suggested before.[19] Nevertheless, it is highly possible that the Zn-rich material in the granules converted to ZnO during sample preparation, via e.g., dissolution of the Zn rich material and crystallization of ZnO.[20]

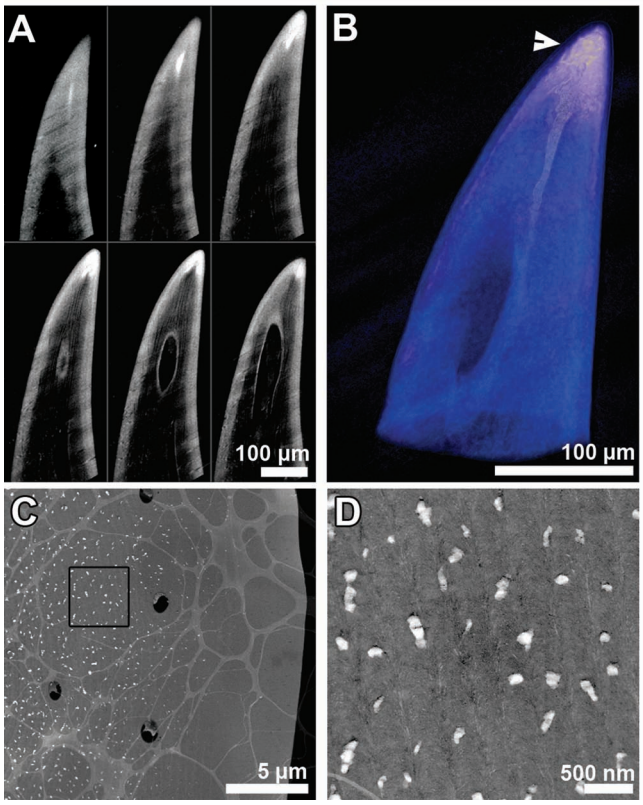

Figure 5. A) A series of high-resolution μCT slices of the fang tip. The brightness stems from higher electron density, corresponding in this case to the localization of Zn, as its absorption cross section is three times larger than that of Ca. B) The brightest signal from all slices is summed and colored in light-yellow, whereas the weaker signal is summed and colored in blue. The yellow region shows the inner Zn-rich cap and the extended protuberance. The arrow head points to the region corresponding to the slice shown in C. C) *Z*-contrast high resolution transmission electron microscopy of a thin section of the fang close to the tip. The signal intensity is related to the atomic mass of the elements in the region, and the sample´s thickness. The bright-grey web-structure forming the background of the image is due to the lacy-carbon support of the TEM grid. The endocuticle in this region contains many granules rich in Zn and with a diameter of 100–200 nm, which are not present in the epicuticle. The black frame corresponds to the area enlarged in (D). D) High magnification of the frame in (C). Note the fiber arrangement in a typical plywood pattern. Brighter regions around the fibers correspond to a concentration of Zn in the protein matrix. In addition granules containing high concentrations of Zn and measuring ≈200 nm in diameter are embedded in the chitin-protein matrix.

2.5. Protein Composition

Amino acid analysis of three subsections of the fang reveals drastic changes in amino acid composition from its tip to its base (Supporting Information Figure 4). Most significantly the content of histidine increases from 3% at the base to 26% at the tip of the fang. Alanine, on the other hand, shows the opposite trend; it decreases from 18% at the base to 7% at the tip. We also compared the amino acid composition of the fang to that of the leg cuticle (tibia); Aspartic acid and aspargine cannot be distinguished in the amino acid analysis. We therefore refer to Asx, which shows a constant concentration of 8% along the fang. This concentration is significantly higher than that in the tibia (2%). The concentration of glycine also remains constant along the entire length of the fang, although at much higher levels (20–24%) than in to the tibia (7%). This is in contrast to the difference in valine and threonine content between the tibia and the fang (20% and 10% in the leg versus >7% and 2% in the fang).

3. Discussion

The fangs of *C salei*, primarily composed of a chitin-protein composite, exhibit notable variations in both organization and local microstructure. The structure of both the epi- and the procuticle is characterized by having microstructural and chemical gradients which give rise to graded mechanical properties, with an over two-fold increase in hardness and a 1.5-fold increase in stiffness from the base to the tip. When compared to classical microstructures known for arthropod cuticles, the fang tip and the bulk of the fang found just distal to the venom canal show extensive structural and chemical adaptations that appear to match their functional need to serve as a puncturing tool. These structural adaptations are summarised in a scheme presented as Supporting Information Figure 5 and discussed below.

3.1. The Chitin

The exocuticle component of the fang exhibits at least two morphologies. One is typical of the outer aspect of the exocuticle and found adjacent to the epicuticle. It is characterized by highly ordered thin lamellae, in which the fibers are coated by a thick protein matrix. This layer encases the entire fang below the epicuticle, and extends all the way down to the base of the fang. The second exocuticlar morphology found more centrally is unusual. It is characterized by highly oriented fiber columns that run parallel to the fang long axis. The highest degree of co-alignment appears in the middle part of the fang whereas the lowest degree of alignment is seen at the fang base. Less specific adaptation is seen in the endocuticle, where the fiber arrangement follows a regular plywood structure with thick lamellae and higher chitin to protein ratios. Overall, the ratio of chitin to protein is low at the fang tip and increases towards the base of the fang. However, the spider fang exhibits gradients of mechanical properties, which do not depend on the chitin content and structural variation alone. We therefore propose that minor components strongly affect the cuticle stiffness and hardness.

3.2. The Proteins

Birkedal et al.[21] reported an increase in glycine and histidine and a decrease in alanine when evaluating the base and tip of the proteinaceous jaws of the polychaete worm *Nereis*. These jaws also contain high levels of Zn and Cl, which these authors proved to be directly related to the mechanical properties of the jaw. Interestingly, a number of glycine- and histidine-rich proteins are reported to be associated with mechanically active hard materials in nature, such as the nematocysts of cnidarians (the stinging cells of jelly fish, corals, etc.), keratins of birds,[22] and the beak and sucker rings of the squid.[23,24] However, in all these cases there is no incorporation of metal ions. An increase in glycine is often related to the stabilization of the intramolecular backbone of the protein by providing sites for hydrogen bonding.[22] Frequently, histidine is involved in intermolecular hydrogen bonding interactions with neighbouring protein side chains. This is achieved by covalent interactions with sclerotizing cross-linking agents[6,8,9] and in particular, in coordination with zinc ions.[25–28] Lichtenegger et al.[27] showed that the average Zn coordination in the *Nereis* jaws consists of three histidine residues and one Cl ion. In the jaw of another polychaete worm, *Glycera*, a similar amino acid distribution was found, but with no traces of Cl which implies a different coordination environment around the Zn ion.[27] In addition, Cu is the more prominent transition metal ion in *Glycera*, which is thought to interact with His.[28,29] Due to the correlation between increased concentrations of both Zn and His at the spider fang tip, we suggest that Zn is involved in intermolecular cross-linking via histidine residues. The difference in the Zn/Cl ratios found in the spider fang suggests either that Zn coordination is not related to Cl, or that more than a single coordination environment exists. In the *Nereis* jaws Zn has only one chemical form, whereas Cl is present both in coordination to Zn, and covalently bound to tyrosine residues (Cl–C).[21,30]

3.3. The Metals

We found both Ca and Zn in the fang. However, as seen in Figure 4, their distribution is very different. The question then arises as to what factors determine the choice of metal ions, and how one may explain the observed metal distribution. Both hardness and stiffness are much higher in the presence of Zn and Cl than in the presence of Ca. We note that their local concentration is also much higher than that of Ca. Nanoindentation measurements alone cannot provide a direct measure for the abrasion resistance, but the ratio $H^{3/2}/Er$ is often used as a first estimation.[29,31] We find a correlation between the $H^{3/2}/Er$ ratio and Zn/Cl enrichment (Supporting Information Table 1), which are both higher in the outer than in the inner layer of the cuticle. Moreover, the ratio seems to drop at the distal part of the fang where the outer layer is enriched with Ca instead of Zn and Cl. This might imply an additional role for Zn and/or Cl in abrasion resistance. It would also be consistent with the widespread occurrence of Zn in the tips of the mandibles and fangs of many invertebrates.[25,32]

The metal-donor (e.g., from protein side chain) bonds of Ca have characteristics different from those of Zn. While the Ca^{2+} ion forms bonds that are mostly ionic (such as with oxygen from Asp or Glu residues or water molecules), the Zn-His coordination complex has a more covalent character and is much shorter (2.03 Å vs. 2.36–2.39 Å).[26] We suspect that the different chemistry associated with Zn, Cl, and Ca might endow the material with different mechanical behavior that is not merely related to its hardness or/and stiffness. The toughness of the material and its viscoelastic properties, which have not been addressed in this study, may play critical roles in the selection of the most appropriate metal ion. The role of Zn-rich granules is still not clear, especially since we are still unsure about their chemistry in the living system. Metal (Fe) rich granules with increased cross-linking density have been shown to significantly increase the hardness of the highly elastic coating of byssal threads of marine mussels.[33] The Zn-rich granules are only present in the chitin-rich region of the fang, such that they may be involved in the cross-linking of matrix proteins surrounding the chitin fibers near the fang tip, thereby facilitating

the transfer of mechanical loads from the matrix to the fibers. Interestingly, the *Glycera* jaws,[28] which like the spider fangs are used to inject venom into prey, contain high levels of copper, which is present both in coordination with the protein matrix as well as in a crystalline mineral form (atacamite).[29]

3.4. The Water

An additional parameter substantially influencing the mechanical properties of cuticle is its water content. All our nanoindentation measurements were performed on dry samples. Our SAM measurements, on the other hand, were always done with hydrated samples and data obtained using both techniques consistently showed the same trends. Similarly, Broomel et al.[34] found no significant difference in the results of nanoindentation experiments performed on the *Nereis* jaws in wet and dry states. And yet, reduction in both hardness and stiffness by 25–35% was observed in the squid beak when measured wet instead of dry.[24] The exocuticular layer of arthropods is usually highly tanned, which suggests that various catechol compounds are incorporated, resulting in heavy cross-linking and an expulsion of water from the tanned cuticle.[35–36] In its natural state, the endocuticle might however contain significant amounts of water. The presence of water is expected to plasticize the protein matrix in the cuticle, but to have little effect on the properties of the chitin fibers themselves. Therefore, the effect of water on the endocuticle must be anisotropic, having the largest effect perpendicular to the fiber axis. As a consequence, the contrast between the endocuticle and the external fang layers increases as observed in comparison between the longitudinal and cross-sections in the SAM images (compare Figure 4A,B).

3.5. The Injection Needle

The fang of *C. salei* is composed of cuticular material that is similar to what is found in the cuticle of the spider´s exoskeleton. And yet the fang contains specialized structural features that have presumably evolved to match the mechanical properties needed to fulfill the function of a multi-use injection needle. The chitin fibers form a scaffold supporting the fangs' structure. The fiber arrangement exhibits the universal plywood architecture with layers oriented parallel to the outer surface. Nonetheless, the typical chitin architecture switches to a more aligned arrangement of fibers close to the fang tip, with the highest degree of alignment seen at the mid-part of the fang. This arrangement corresponds to the expected strain trajectories that develop in the fang when it hits its target. The fang's protein composition seems to be specialized with reduced amounts of Val and Thr, which are largely replaced by Gly and Asx. The major adaptations are found in the fang's tip. First, the tip is enriched with protein with a high content of His. Interestingly, similar His- and Gly-rich protein compositions were described for structural proteins in other load bearing materials with[21,27,30] or without metal ion incorporation.[22,23] In the spider fang, the His-rich protein clearly correlates with an increase of the Zn ion concentration, which suggests that the strength of the protein stems from Zn-His cross-linking. In addition, the chitin-protein composite in the tip is reinforced by granules sized 200 nm in diameter with even higher Zn content as compared with the Zn concentration in the surrounding protein matrix. We believe that the combination of these compositional modifications entail the high values of hardness and stiffness found at the fang tip. For comparison, values of 0.7 GPa for hardness and 12 GPa for indentation modulus are reported for *Nereis* jaws,[27] while *Glycera* jaws, which contain atacamite, have a hardness of $H_{max} = 1.3$ GPa, similar to *C. salei*, with a slightly lower indentation modulus $Er_{max} = 17.7$ GPa.[29]

The process of needle insertion in general includes two stages.[37,38] The needle is first pressed onto the surface, which is that of the prey's exoskeleton in our case, generating forces near the tip and deforming the surface.[37,38] At this stage large stresses are expected to concentrate at the tip of the fang.[39] When a threshold force is reached, the prey's cuticle ruptures and cracks, allowing the needle to penetrate into the medium.[37,40] In the life time of the spider, the fang is repeatedly exposed to such increased mechanical loads from both the initial impact and during the puncture of the prey's cuticle. The major loads are taken by the fang tip with its specialised structure and composition. Interestingly, the (Zn-rich) hard part of the fang extends distally from the opening of the venom canal and seems to be anchored into the chitin scaffold by elongated protuberances. This reinforcement could be a protection against fracture at this otherwise weak area. The two serrated ridges at the ventral side of the fang might play a role during the second stage of needle insertion, by cutting through the prey's fibrous cuticle. As friction forces also play a significant role,[41] the possibility that the many pores at the tip of the fang are related to the secretion of lubricating material is under consideration.

4. Conclusion

Chitin has long been considered to be a key player determining the mechanical properties of biomaterials of various groups of invertebrate animals as discussed previously.[5] A growing number of studies have stressed the importance of the protein matrix in determining the mechanical properties of the composite.[5,24,42,43] The spider fang shows that both components play important mechanical roles. Chitin acts primarily as a load-bearing scaffold supporting the structure and entails bending stiffness. The proteins, on the other hand, exhibit higher chemical variability and can easily be modified chemically. It is presumably for this reason that the regions of the fang that carry the largest stress upon interaction with the spider prey, i.e., the tip of the fang and the outer layer, consist mainly of protein, and the outer layer of the exocuticle contains a remarkably thick protein matrix. Possible modifications of the cuticular proteins include e.g., halogenations, diverse types of cross-links with different metal ions, sclerotization by the introduction of catechols, and specific stereochemical interactions such as observed for the chitin-binding domains.[11,21,30,35,43,44] The spider takes advantage of a wide range of the available chemical and structural modifications in its cheliceral fangs. These have a highly specialized tip structure, an external layer with high abrasion resistance and graded properties from base to tip. The spider fangs therefore offer a unique opportunity to study the

effects of such modifications within one system and make it possible to understand the role such modifications have in fine tuning the mechanical properties of the arthropod cuticle in general. These features could perhaps also serve as lessons for the design of injection needles with specialized morphologies and properties which could obviously be of great interest for example in medical applications.

5. Experimental Section

Spider Material: Adult specimens of the Central American wandering spider *Cupiennius salei* Keys. (*C. salei*) were obtained from the breeding stock of the Department of Neurobiology of the University of Vienna. The spiders were stored in ethanol (70%) at 8 °C for periods of up to one month. The fangs were dissected away from the chelicerae, washed shortly with deionized water and air dried. For high-resolution SEM (HR-SEM, JEOL JSM7500F) dry fangs were mechanically fractured, mounted on an SEM-sample holder with conductive carbon tape and sputtered with Au/Pd.

Sample Embedding and Preparation: Isolated fangs were immersed for 8 h in methylmetacrylate (MMA) and polymerized in an oven at 60 °C. For the synchrotron X-ray SAXS/XRD measurements, the embedded samples were cut with a diamond saw (Leica SP1600 saw-microtome) into 200 µm thick cross or longitudinal sections. For SAM, nanoindentation and energy dispersive spectroscopy (EDS) cross and longitudinal sections were cut using a Leica microtome (Leica SM2500E, Leica Microsystems, Bensheim, Germany) and polished lightly anhydrously. The samples were initially used for nanoindentation measurements, re-polished, and subsequently SAM imaged followed by EDS analysis in the SEM.

Acoustic Microscopy: Polished sections were imaged using a scanning acoustic microscope (SAM, Krämer Scientific Instruments, SAMTEC GmbH Evolution PII series). Deionized de-gassed water served as the coupling medium. Images were obtained using a lens frequency of 860 MHz with an aperture angle of 100°.

Element Analysis: Following SAM imaging, the section samples were mounted on an SEM stub with conductive carbon paint (SPI Supplies), carbon coated, and analyzed in an SEM. EDS analysis was performed in a LEO 1550 Field Emission SEM (Carl-Zeiss AG, Germany) equipped with X-Max80 Large Area SDD, silicon drift detector (SDD) (Oxford Instruments, UK), operated by INCA Energy 350 EDX-system. The microscope was operated at 20 KeV, with a working distance of 8 mm.

SAXS, XRD, and XRF Mapping: Embedded thin samples were measured at the dedicated station for scanning SAXS/WAXS/XRF of the µ-Spot beamline at the BESSY II storage ring (HZB: Helmholtz Center Berlin for Materials and Energy). A beam energy of 15 KeV (λ = 0.826 nm) was defined using a multilayer monochromator. The beam was focused on the sample with a torroidal mirror, and the final beam size was defined by a pinhole of 10 µm diameter behind the sample. SAXS/WAXS data was obtained simultaneously in transmission mode using a large-area 2D charge coupled device (CCD) detector (MarMosaic 225, Mar USA Evanston, USA) situated approximately 380 mm away from the sample. For simultaneous XRF measurements, an energy dispersive detector (ASAS-SDD, KETEK, Germany) was positioned approximately 60° to the X-ray beam axis. The sample to detector distance was calibrated using crystalline silver behenate powder. For radial and azimuthal integration and reduction of the 2D images into profiles, the software Fit2D[45] was used.

For each SAXS pattern, the particle degree of co-alignment (ρ) was calculated within the range of $Q = 1.26$–1.3 nm^{-1}, using $\rho = A_1/(A_1 + A_0)$, where A_0 is the total SAXS intensity of the chitin fibers and A_1 depicts the SAXS intensity of the fibers exhibiting a preferred orientation in the plane of the detector. The ρ-parameter ($0 < \rho < 1$) provides a direct measure of the degree of co-alignment of the fiber crystals, such that $\rho = 0$ means that the fibers are randomly oriented in the scattering volume whereas $\rho = 1$ indicates that all the fibers in the scattering volume have the same average orientation.[18]

Nanoindentation: Embedded and polished samples were measured with a UB1 nanoindenter (Hysitron, Minneapolis, MN, USA), using a Berkovich tip. The load function was chosen as in ref. [34] loading/unloading rate of 100 µN s^{-1} with a holding time at peak load of 500 µN for 60 s were used. Data were collected in open-loop mode with 1026 points per indent. Load–displacement curves were analyzed for reduced *Er* and *H* according to the Oliver and Pharr method.[46] Property maps were generated using Origin (OriginLab V 8.0, Northampton, MA, USA). Calibrated grey level maps were exported to ImageJ software (National Institute of Health, USA) and averages of inner and outer layers were determined using the Histogram analysis'tool.

HR-TEM: 70–100 nm thin slices of air dried fang samples were prepared with an ultramicrotom (Leica EM UC6). The slices were mounted on lacy-carbon support gold TEM grids and viewed with a HR-TEM (TITAN 80-300) in Z-contrast scanning-transmission mode (STEM).

Amino Acid Analysis: The amino acid composition of three segments of the fang were determined by Genaxxon bioscience GmbH using amino Acid Analyser LC3000. Several fangs were air-dried and sectioned into 3 parts. The content of the venom canal was gently removed with tweezers. Each sample was supplemented with HCl (600 µL 6 N), sealed under vacuum (<20 mbar) and hydrolyzed for 96 h at 110 °C. After hydrolysis, samples were dried at 36°C for 4 h (vacuum centrifuge). Each dried sample was supplemented with Na-Acetat buffer (500 µL, pH = 2.2) for subsequent derivatization and high pressure liquid chromatography (HPLC; polymeric cation exchange column). Fragmented amino acids were detected by post-column Ninhydrin derivatisation at 125 °C and photometric measurement at 570 nm. Data was monitored by the chromatography software ChromStar 6.0. following calibration of the HPLC using a commercial standard (Sigma-Aldrich, A2908).

Monochomatic Absorption-Contrast µCT: A dry fang was mounted upright on the rotation stage of the microtomography setup of the BAMline imaging beam line of BESSY II storage ring (HZB Helmholtz Center Berlin for Materials and Energy.[47] 600 radiographs were recorded at angular increments of 0.3° using an energy of 20 KeV ($\Delta E/E = 0.5\%$) in absorption mode. The projection images had an effective pixel size of 0.89 µm and were normalized and reconstructed using the ESRF python code PyHST (ESRF, Grenoble France) and then visualized, rotated, and cropped (Amira 5.1, Visage Imaging GmbH, Germany, and Drishti Volume Exploration and Presentation Tool, http://anusf.anu.edu.au/Vizlab/drishti/).

Supporting Information

Supporting Information is available from the Wiley Online Library or from the author.

Acknowledgements

The authors thank Maria Wieser, Elisabeth Fritz-Palank, and Miroslav Dragasev of Vienna University who kindly helped with the animal material. They would like to thank Annemarie Martins, Birgit Schonert, and Rona Pitschke for help in sample preparation; Petra Leibner and Christine Pilz-Allen for help with nanoindentation and SAM; and Heinrich Risermeier and Ralf Britzke for access and assistance with BAMline of the HZB. The authors thank Dr. Matthew Harrington and Dr. Christopher Broomell for invaluable discussions and Michael Kerschnitzki for help in video preparation. Y.P is funded by an Alexander von Humboldt Research Fellowship for Postdoctoral Researchers.

Received: January 9, 2012
Published online: March 22, 2012

[1] J. F. V. Vincent, *Compos. Part A* **2002**, *33*, 1311.
[2] F.G. Barth, *A Spider's World: Senses and Behavior*, Springer-Verlag, Berlin, Heidelberg, New York **2002**.
[3] F. G. Barth, *Zoology* **2002**, *105*, 271.
[4] F.G. Barth, *Z. Zellforschung* **1973**, *144*, 409.
[5] *Biology of the Integument 1, Invertebrates*, (Eds: J. Bereiter-Hahn, G. A. Matoltsy, S. K. Richards), Springer-Verlag, Berlin, Heidelberg **1984**.
[6] G. Fraenkel, K. M. Rudall, *Proc. R. Soc. London, Ser. B* **1947**, *134*, 111.
[7] A C. Neville, D. A. Parry, J. Woodhead-Galloway, *J. Cell Sci.* **1976**, *21*, 73.
[8] J. H. Willis, *Integr. Comp. Biol.* **1999**, *39*, 600.
[9] V. A Iconomidou, J. H. Willis, S. J. Hamodrakas, *Insect Biochem. Mol. Biol.* **2005**, *35*, 553.
[10] S. J. Hamodrakas, J. H. Willis, V. A. Iconomidou, *Insect Biochem. Mol. Biol.* **2002**, *32*, 1577.
[11] J. Blackwell, M. A Weih, *J. Mol. Biol.* **1980**, *137*, 49.
[12] E. Atkins, *J. Biosci.* **1985**, *8*, 375.
[13] S. Andersen, M. Peter, P. Roepstorff, *Comp. Biochem. Physiol. B: Biochem. Mol. Biol.* **1996**, *113*, 689.
[14] Y. Bouligand, *Tissue Cell* **1972**, *4*, 189.
[15] M. M. Giraud-Guille, *Tissue Cell* **1984**, *16*, 75.
[16] J. F. V. Vincent, U. G. K. Wegst, *Arthropod Struct. Dev.* **2004**, *33*, 187.
[17] A. G. Richards, *Zoologische Jahrbücher, Abteilung Anatomie und Ontogenie der Tiere* **1967**, *84*, 25.
[18] W. Wagermaier, H. S. Gupta, A. Gourrier, O. Paris, P. Roschger, M. Burghammer, C. Riekel, P. Fratzl, *J. Appl. Crystallogr.* **2007**, *40*, 115.
[19] Y. Tao, J. Shokes, R. A. Scott, M. Nesson, R. M. S. Schofield, in X-ray Absorption Fine structure–XAFS13 13th International Conference, Stanford, CA, USA, July 9-14, 2006, *Am. Inst. Phys.* **2007**, 352.
[20] S. Cho, J.-W. Jang, A. Jung, S.-H. Lee, J. Lee, J.S. Lee, K.-H. Lee, *Langmuir* **2011**, *27*, 371.
[21] H. Birkedal, R. K. Khan, N. Slack, C. C. Broomell, H. C. Lichtenegger, F. Zok, G. D. Stucky, J. H. Waite*ChemBioChem* **2006**, *7*, 1392.
[22] W. Koch, T. W. Holstein, C. Mala, E. Kurz, J. Engel, C. N. David, *J. Cell Sci.* **1998**, *111*, 1545.
[23] A. Miserez, T. Schneberk, C. Sun, F. W. Zok, J. H. Waite, *Science* **2008**, *319*, 1816.
[24] A. Miserez, J. C. Weaver, P. B. Pedersen, T. Schneeberk, R. T. Hanlon, D. Kisailus, H. Birkedal, *Adv. Mater.* **2009**, *21*, 401.
[25] C. C. Broomell, R. K. Khan, D. N. Moses, A. Miserez, M. G. Pontin, G. D. Stucky, F. W. Zok, J. H. Waite, *J. R. Soc. Interface* **2007**, *4*, 19.
[26] M. M. Harding, M. W. Nowicki, M. D. Walkinshaw, *Crystallogr. Rev.* **2010**, *16*, 247.
[27] H. C. Lichtenegger, T. Schöberl, J. T. Ruokolainen, J. O. Cross, S. M. Heald, H. Birkedal, J. H. Waite, G. D. Stucky, *Proc. Natl. Acad. Sci. USA* **2003**, *100*, 9144.
[28] H. C. Lichtenegger, H. Birkedal, D. M. Casa, J. O. Cross, S. M. Heald, J. H. Waite, G. D. Stucky, *Chem. Mater.* **2005**, *17*, 2927.
[29] H. C. Lichtenegger, T. Schöberl, M. H. Bartl, H. Waite, G. D. Stucky, *Science* **2002**, *298*, 389.
[30] R. K. Khan, P. K. Stoimenov, T. E. Mates, J. H. Waite, G. D. Stucky, *Langmuir* **2006**, *22*, 8465.
[31] M. G. Pontin, D. N. Moses, J. H. Waite, F. W. Zok, *Proc. Natl. Acad. Sci. USA* **2007**, *104*, 13559.
[32] R. M. S. Schofield, *J. Insect Physiol.* **2003**, *49*, 31.
[33] M. J. Harrington, A. Masic, N. Holten-Andersen, J. H. Waite, P. Fratzl, *Science* **2010**, *328*, 216.
[34] C. C. Broomell, M. A. Mattoni, F. W. Zok, J. H. Waite, *J. Exp. Biol.* **2006**, *209*, 3219.
[35] M. G. M. Pryor, *Proc. R. Soc. London, Ser. B* **1940**, *128*, 378.
[36] T. L. Hopkins, K. J. Kramer, *Ann. Rev. Entomology* **1992**, *37*, 273.
[37] L. Barbe, B. Bayle, M. Demathelin, A. Gangi, *Biomed. Signal Process. Control* **2007**, *2*, 191.
[38] S. Misra, K. B. Reed, B. W. Schafer, K. T. Ramesh, A. M. Okamura, *Int. J. Rob. Res.* **2010**, *29*, 1640.
[39] K. Oka, S. Aoyagi, Y. Arai, Y. Isono, *Sens. Actuators, A* **2002**, *98*, 478.
[40] O. A. Shergold, N. A. Fleck, *Proc. R. Soc. London, Ser. A* **2004**, *460*, 3037.
[41] A. M. Okamura, C. Simone, M. D. O'Leary, *IEEE Trans. Biomed. Eng.* **2004**, *51*, 1707.
[42] J. F. V. Vincent, *Composites Part A* **2002**, *33*, 1311.
[43] J. E. Hillerton, J. F. V. Vincent, *Int. J. Biol. Macromol.* **1983**, *5*, 163.
[44] S. O. Andersen, P. Hojrup, P. Roepstorff, *Insect Biochem. Mol. Biol.* **1995**, *25*, 153.
[45] A. P. Hammersley, S. O. Svensson, A. Thompson, *Nucl. Instrum. Meth.* **1994**, *A346*, 312
[46] W. C. Oliver, G. M. Pharr, *J. Mater. Res.* **1992**, *7*, 1564.
[47] A. Rack, S. Zabler, B. Muller, H. Riesemeier, G. Weidemann, A. Lange, J. Goebbels, M. Hentschel, W. Gorner, *Nucl. Instrum. Methods Phys. Res., Sect. A* **2008**, *586*, 327.